JOURNAL OF COMPUTATIONAL PHYSICS 38, 378–395 (1980)

A Global Method of Solving the Electron–Field Equations in a Zero-Inertia-Electron-Hybrid Plasma Simulation Code*

D. W. HEWETT

Los Alamos Scientific Laboratory, University of California, P. O. Box 1663, Los Alamos, New Mexico 87545

Received August 27, 1979

A formulation of the electron momentum equation and Maxwell's field equations suitable for global solution in an r–z hybrid plasma simulation code has been derived. The assumption of zero electron inertia is made in the electron momentum equation and Maxwell's equations are used in the radiation-free or Darwin limit. These techniques make explicit use of the axisymmetric properties of the model to decouple the components of the model equations. Equations to self-consistently advance the electron temperature are not presently included in this scheme. The model equations which result from these considerations are two coupled, nonlinear, second order partial differential equations. These two equations are integrated in time by a noniterative ADI procedure along with the explicit particle-in-cell ion time integration procedure. The resulting nearly implicit electron–field algorithm treats wide variations in the local signal velocity without instability; this consideration is most important since pure vacuum regions are allowed. The global nature of the solution requires boundary conditions only on the boundaries of the simulation region; arbitrary intermixing of plasma vacuum regions requires only the simple detection of low density cells and does not require monitoring of plasma vacuum interfaces.

A plasma simulation method which can describe macroscopic phenomena while including particle ion effects in high-β plasmas has considerable utility in evaluating magnetic fusion concepts. Of particular interest are plasma phenomena having gradient scale lengths comparable to ion gyroradii which are both on the order of centimeters and time scales on the order of a few tens of microseconds or longer. Examples of plasmas with such parameters abound in high-β controlled fusion research with typical plasma parameters ranging between 10^{14} and 10^{17} particles/cm^3 for densities, between 1 and 7 keV for temperatures, and between 10 and 50 kG for magnetic fields. Multidimensional simulation of such plasmas has until recently been restricted to models describing only MHD behavior and therefore has not included all the physical effects desired. Conversely, full electron and ion particle-in-cell techniques provide more details about plasma behavior than are needed for macroscopic studies; such methods follow plasma behavior on electron time and length scales which, for plasmas of interest in this work, are on the order of 10^{-12} sec and 10^{-10} cm, respectively—far too microscopic for practical extension to plasmas under consideration now.

* Work performed under the auspices of the U. S. Department of Energy, under Contract W-7405-Eng. 36. The U. S. Government's right to retain a nonexclusive royalty-free license in and to the copyright covering this paper, for governmental purposes, is acknowledged.

0021-9991/80/150378-18$02.00/0

What is needed is a hybrid model which describes plasmas with a level of detail between these two extremes. Several potentially useful multidimensional models have recently been developed for simulation in this parameter regime. The model of Okuda *et al.* [1] assumes the electrons are always in thermodynamic equilibrium and thus form a Debye sheath about the equilibrium ion density. The model is quite successful in simulating low frequency ion oscillations and eliminates high frequency fluctuations. Resistive heating effects may be difficult to include since extension of the model to nonadiabatic electrons appears to be problem dependent. Another model which approaches the required parameter regime is the finite electron mass model of Hewett and Nielson [2]. Through separation of the electron current and electric field into irrotational and solenoidal components, electron plasma oscillations and the associated time step restrictions are eliminated from the model. Other electron inertial effects necessary to describe most microinstabilities requiring finite ω_{ce} are retained. This model, however, retains a fraction of the ω_{ce} time step constraint, depending upon the magnitude of **B** in the simulation plane, and consequently is primarily useful for studying microinstabilities not requiring ω_{pe} effects. The ω_{ce} constraint is still too restrictive ($\omega_{ce} = 10^{-12}\,\text{sec}^{-1}$ for typical plasmas of interest here) for microsecond time scales.

A model by Byers *et al.* [3] appears to provide an avenue of approach to the desired parameter regime. Their model utilizes CIC techniques for the ion component coupled with a zero mass fluid model to represent the electrons. Quite complete linearized stability analyses were carried out for various versions of this model. Hewett and Sgro [4] have implemented and extended a very similar model in two-dimensional (r–z) geometry which has provided useful simulations of the dynamics of a bumpy θ-pinch implosion. One source of difficulty is that these hybrid techniques all use the electron and field equations in a manner which requires division by the density in each plasma computational cell. This feature produces sensitivity to fluctuations in regions of low but finite density and will not describe regions with zero density. To model bumpy θ-pinch behavior, Hewett and Sgro made provisions for a separate vacuum treatment of regions in which density falls below a cutoff level. Ultimately, in the Hewett and Sgro version, numerical instabilities arising from violation of multidimensional stability constraints were encountered in the attempt to simulate phenomena having shorter axial wavelengths. Additionally, some difficulties were encountered when the regions of plasma and vacuum became highly intermixed, such as occurs in the dynamical stages of plasma implosions.

In this paper, a new method of solution for the relevant combination of electron and radiationless field equations is proposed. Though presently implemented with a non-self-consistent electron temperature, this formulation appears to have greatly reduced the difficulties associated with low density fluctuations as well as allowing arbitrary plasma–vacuum intermixing *without* having the monitor the location of plasma–vacuum interfaces. Simulations for the purpose of testing field calculations have been made in which regions of finite plasma density are represented by only one or two particles per cell without introducing catastrophic instability. Obviously the physics described with such a minimal representation is at best questionable, but the

robustness required to handle stochastic plasma–vacuum boundaries is clearly demonstrated. The surprisingly good performance in the presence of high fluctuations is attributed to the nearly implicit field–electron current calculation. It is also this property which allows the freedom to specify boundary conditions only on the simulation boundaries regardless of the distribution of density within the region. Furthermore, the implicit form does not exhibit the numerical instability associated with the small grid spacing in the axial direction found in the earlier version [4]. The practical time step constraint is that no ion velocity or hydromagnetic wave associated with the minimum finite density allowed (or density "cutoff" value) may travel more than one cell in one time step. Further discussion of these properties will be given in the following sections, in which the model is developed, and in the application section, in which the first applications of the method are discussed.

Derivation of the Global Field Equations

The basic equations for advancing the electromagnetic fields in any simulation are of course Maxwell's equations. However, the zero electron inertia assumption provides additional constraints which must be utilized to self-consistently advance the electron quantities, such as current $\mathbf{J}_e$ and temperature T_e, simultaneously with the field components. What results is a mixture of the electron momentum equation and Maxwell's equations which must be advanced in time along with the ion particle advance. These electron–field equations are configured for this work to allow nearly implicit time advance of all field and electron quantities in axisymmetric cylindrical geometry. In the following derivation it is assumed that all ion source terms, such as number density ρ and current $\mathbf{J}_i$, are available at time level $t = n\,\Delta t$ from the most recent pass through the particle-in-cell routines as well as the field components at the previous time level.

In the limit of small electron inertia, the electron momentum equation is

$$\mathbf{E} = -\frac{\nabla \rho T_e}{e\rho} - \frac{\mathbf{u}_e \times \mathbf{B}}{c} + \boldsymbol{\eta} \cdot \mathbf{J}, \tag{1}$$

where T_e and $\mathbf{u}_e$ are the electron temperature and drift velocity, respectively. $\mathbf{E}$ and $\mathbf{B}$ are the electromagnetic fields, $\mathbf{J}$ is the total current, $\boldsymbol{\eta}$ is the resistivity, e is the electronic charge, and c is the velocity of light. Quasi-neutrality is assumed in this model so that the electron density is nearly equal to the ion density and both will be denoted by the symbol ρ.

An immediate consequence of quasi-neutrality is that the total current $\mathbf{J}$ must be nearly solenoidal, $\mathbf{J} \cong \mathbf{J}_t$. The subscript t here denotes a solenoidal (transverse) vector

and the subscript l denotes an irrotational (longitudinal) vector. This result follows from the charge continuity equation which, in the quasi-neutral limit, is

$$\nabla \cdot \mathbf{J}_e \cong -\nabla \cdot \mathbf{J}_i. \tag{2}$$

This equation suggests the choice of equal and opposite irrotational currents $\mathbf{J}_{el} = -\mathbf{J}_{il}$ which is fully general as long as the boundary conditions on the currents are consistent with quasi-neutrality.

To complete the set of equations governing the time advance of electron–field quantities, the radiation-free or Darwin limit of Ampere's law

$$\nabla \times \mathbf{B} = \frac{4\pi}{c} \mathbf{J}_t \tag{3}$$

and Faraday's law

$$\nabla \times \mathbf{E}_t = -\frac{1}{c} \frac{\partial \mathbf{B}}{\partial t} \tag{4}$$

must be combined with the electron momentum equation (1). Introducing the magnetic vector potential $\mathbf{A}$ in the Coulomb gauge, Eq. (1) takes the form

$$\dot{\mathbf{A}} = c \frac{\nabla p_e}{e\rho} + c\mathbf{E}_l + \mathbf{u}_e \times \mathbf{B} - \frac{c^2}{4\pi} \boldsymbol{\eta} \cdot (\nabla \times \mathbf{B}), \tag{5}$$

where the relation $\mathbf{E}_t = -\dot{\mathbf{A}}/c$ has been used. Since $\mathbf{B} = \nabla \times \mathbf{A}$, Eq. (5) would provide an explicit method of advancing $\mathbf{B}$ if a convenient method of determining $\mathbf{u}_e$ and $\mathbf{E}_l$ could be found. Solving the quasi-neutral Poisson equation [2] is one possibility for finding E_l. It is simpler, however, to exploit the axisymmetry of the model in the present case. In this model $\partial/\partial\theta \equiv 0$ so that the θ-component of $\mathbf{E}_l$ is identically zero. Therefore only the θ-component of Eq. (5),

$$\dot{A}_\theta - \frac{c^2}{4\pi} \eta_{\theta\theta} \nabla^2 \mathbf{A}\Big|_\theta + u_{er} \frac{1}{r} \frac{\partial (rA_\theta)}{\partial r} + u_{ez} \frac{\partial A_\theta}{\partial z} + ce\rho[\eta_{\theta r}(u_{ir} - u_{er}) + \eta_{\theta z}(u_{iz} - u_{ez})] = 0, \tag{6}$$

is solved. A_θ and, consequently, B_r and B_z are advanced in time using this equation with u_{er} and u_{ez} coming from the curl of $B_\theta \hat{e}_\theta \rho$, u_{ir}, and u_{iz}.

What remains to be found is a procedure for advancing B_θ in time. Equation (6) provides for evaluating $\dot{A}_\theta$ in terms of A_θ^{n-1} and B_θ^{n-1} and other quantities known from the particle advance. What is needed is an expression for $\dot{B}_\theta$ in terms of A_θ^{n-1} and B_θ^{n-1} and known quantities. This relation can be obtained by first taking the curl of Eq. (1) and then replacing $\nabla \times \mathbf{E}$ with $\dot{\mathbf{B}}$ from Faraday's law equation (4). The θ-component of the resulting equation is

$$\dot{B}_\theta - \frac{c^2}{4\pi}\left[\frac{\partial}{\partial r}\frac{\eta_{zz}}{r}\frac{\partial(rB_\theta)}{\partial r} + \frac{\partial}{\partial z}\eta_{rr}\frac{\partial B_\theta}{\partial z}\right] + \frac{\partial}{\partial r}[u_{er}B_\theta] + \frac{\partial}{\partial z}[u_{ez}B_\theta]$$

$$- c\left[\frac{\partial}{\partial r}\{ep[\eta_{zr}(u_{ir} - u_{er}) + \eta_{z\theta}(u_{i\theta} - u_{e\theta})]\}\right.$$

$$\left. - \frac{\partial}{\partial z}\{ep[\eta_{r\theta}(u_{i\theta} - u_{e\theta}) + \eta_{rz}(u_{iz} - u_{ez})]\}\right]$$

$$= B_r\left[\frac{\partial u_{e\theta}}{\partial r} - \frac{u_{e\theta}}{r}\right] + B_z\frac{\partial u_{e\theta}}{\partial z} - \frac{c}{ep}\left[\frac{\partial p}{\partial z}\frac{\partial T_e}{\partial r} - \frac{\partial p}{\partial r}\frac{\partial T_e}{\partial z}\right]. \tag{7}$$

To complete this model, a mechanism for advancing T_e which can proceed along with the other time integration procedures is required. Since electron phenomena are assumed in this model to occur on time scales much shorter than a time step in the code, standard techniques for advancing the electron temperature are not appropriate. Methods of advancing T_e which correctly express, for example, the rapid thermal equilibration along field lines require a solution technique which expresses the idea of instantaneous thermal equilibration rather than temporal advance by electron convection. This problem requires more than a simple evaluation of $\partial T_e/\partial t$, and several methods are now under consideration. For present purposes, it is assumed that T_e is not advanced in a self-consistent manner. It is noted that a procedure to advance T_e as a function of plasma and field quantities

$$\dot{T}_e = f(\rho, T_e, \mathbf{u}_e, \mathbf{B}, \eta) \tag{8}$$

is all that is required to fit into this numerical scheme. For the model tests presented later, T_e is assumed to be a uniform constant 1 eV.

Equations (6) and (7) thus comprise a set of coupled nonlinear partial-differential equations which can be used to advance the magnetic field in time along with the associated electron current. The completeness of this set is demonstrated by the fact that given ion source terms, the temporal behaviors of A_θ and B_θ are expressible as functions of only themselves.

Regions of Small or Zero Density

As mentioned previously, one of the most common difficulties with earlier codes with similar physics is the problem of low density fluctuations. Since Eqs. (6) and (7) are both formulated in terms of the electron drift velocity $\mathbf{u}_e$, the difficulty is largely shifted to equations for $\mathbf{u}_e$, which are

$$u_{er} = u_{ir} + \frac{c}{4\pi ep}\frac{\partial B_\theta}{\partial z}, \tag{9a}$$

$$u_{e\theta} = u_{i\theta} + \frac{c}{4\pi e\rho} \nabla^2 \mathbf{A} \Big|_{\theta}, \tag{9b}$$

$$u_{ez} = u_{iz} - \frac{c}{4\pi e\rho} \frac{1}{r} \frac{\partial (rB_\theta)}{\partial r}. \tag{9c}$$

For a cell with zero density, the equations appear to break down. No difficulty is encountered, however, since, if $\rho = 0$ in a cell, $\mathbf{J}$, $\mathbf{u}_i$, and $\mathbf{u}_e$ are also zero. Numerical problems do appear in cells with small but finite density. A density fluctuation resulting from the relatively small number of simulation particles is clearly an aberration which has no physical meaning considering the large absolute densities of even the lowest density experimental plasmas. When encountering a low density fluctuation, simulation algorithms generate a spike in the local density-dependent signal velocity. Typically, this velocity spike can exceed the local Courant stability limit [6] which causes an abrupt termination of the simulation. While an understanding of such phenomena is satisfying, the abrupt termination of the simulation is clearly unacceptable.

One possible solution is to postulate a finite density (or cold background plasma) in each cell to provide a lower limit on ρ and thus eliminate the velocity spike. Unfortunately, a numerically significant background density in a true vacuum region produces an unacceptable alteration of the desired physics—particularly in the case of time-dependent external fields propagating nearly instantaneously across a vacuum region. What appears to be required is a method for distinguishing between true vacuum regions, perhaps just forming, and low density fluctuations. If this distinction could be made, the method could insert a background density in the "fluctuation" cells and treat separately the true vacuum regions. A sufficiently clever algorithm would be hard to describe. Additionally, if the model treats plasma and vacuum regions separately, a time-explicit algorithm must monitor, if not store, the location of plasma–vacuum interfaces. For a highly turbulent situation such as one might encounter in a plasma gun, for example, monitoring the plasma–vacuum interfaces becomes quite complicated and time consuming, if not impossible.

The conclusion that emerges is that it is highly desirable to consider techniques which can handle the disparity in signal velocities in adjacent cells and not require the algorithm to define separate plasma and vacuum regions. Such difficulties are frequently encountered in other areas of numerical simulation and are commonly overcome by treating the time advance of the offending equations implicitly [6]. This numerical technique allows unwanted high frequency phenomena to decay exponentially with time. These implicit schemes have the property of being unconditionally stable in the simpler linear applications. Nonlinear applications generally are not totally without stability bounds but can usually be characterized as being more robust than their explicit counterparts.

Before attempting to solve Eqs. (6) and (7) with an implicit algorithm, several other issues must be considered. Since it is not practical to advance the particle ion component in time implicitly, the explicit particle-in-cell technique will impose a time

step constraint on the total algorithm. This constraint typically implies that the ion thermal and flow velocities as well as wave phenomena carried by the ions travel not more than a cell length in a time step [6]. Such restrictions serve as practical limitations for the time step size in accurate simulations. Consequently, even though an implicit electron–field algorithm is theoretically capable of handling arbitrarily small but finite densities (hence arbitrarily large signal velocities), there is no advantage to achieving this level of performance in nonvacuum regions considering the time step constraint imposed by the ions. Therefore, no penalty is incurred by imposing a minimum density "cutoff" value—below which the cell is considered to be vacuum—to reduce the signal velocity magnitudes which the algorithm must handle. Practically, the cutoff value is chosen small enough to insure that all but 2 or 3% of the particles are included in "plasma" cells. Cutoff values greater than a few percent make the distinction between plasma and vacuum regions questionable.

With the introduction of a density minimum in combination with the explicit ion advance, the need for an implicit electron–field algorithm may seem less compelling. Any advantage gained by integrating these equations implicitly in time is in principle restricted to time scales faster than typical ion flow and wave propagation times through a cell since this time scale must be resolved by the time step anyway. However, the more robust implicit method is much more tolerant of locally extreme fluctuations in these velocities than the corresponding explicit algorithm. More importantly, the implicit procedure handles the disparity in signal velocities between adjacent plasma and vacuum cells without instability. The only distinction between a true vacuum region's first appearance and a fluctuation "vacuum" is simply that the true region will persist while the fluctuation is likely to disappear after the next particle time step. In addition, the capability to handle the occurrence of a zero density or vacuum cell stochastically imbedded in the "finite density" plasma region without imposing a finite background density is also achieved. Again, the importance of this feature is apparent in that the propagation speed of electromagnetic phenomena across vacuum regions is infinite in this model.

With the exception of Eqs. (9) the implicit time advance of the electron–field equations removes the need for separate treatments of plasma–vacuum regions and therefore the need for interface monitoring. Equations (6) and (7) automatically respond with the appropriate physics in regions of low or zero density. In a vacuum cell, Eq. (6) reduces to $\nabla^2 \mathbf{A}|_\theta = 0$ and, with proper concern for the difference scheme, Eq. (7) is made to reduce to $-\nabla^2 \mathbf{B}|_\theta = \nabla \times B_\theta \hat{e}_\theta = 0$—the physically correct vacuum equations. This response is a consequence of the approximation of infinite vacuum resistivity in which η is set to a large ($\eta_{\text{plasma}} \times 10^{10}$) value in any cell in which the density drops below the cutoff value. Thus, terms in Eqs. (6) and (7) containing η dominate other terms in the equations and automatically reduce to the desired limit. As a result, the **B** field advance can function properly with boundary conditions applied only on the boundaries of the simulation region. There are no restrictions on the position or number of plasma–vacuum interfaces.

The total **E** field in finite density cells is now calculated from Eq. (1) using the newly updated **B** field and $\mathbf{u}_e$. The field calculations are completed by solving

$\nabla^2 \mathbf{E} = 0$ in the vacuum region [4] by a separate routine employing adaptive ADI [7]. This routine is arranged so that the **E** field solution obtained from Eq. (1) in regions of finite density is preserved. In regions of low or zero density, the routine shifts automatically to a five-point vector Poisson algorithm.

To conclude this section on the low density problem, the following comments should be noted. Even with large numbers of simulation particles, the possibility of a cell with small but finite density always exists due to the nature of PIC simulation. Such cells are inevitable if vacuum regions and their associated interfaces are allowed to move. The question is often raised concerning the correctness of not distinguishing true vacuum regions from stochastic "vacuum" cells within regions of finite density. Since *something* must be done to determine the fields in these cells, it is reassuring to see that the procedures discussed in this section could equally well be described as simply the "patching over" of the offending region by averaging the nearest neighbor field quantities with a five-point Poisson operator.

Numerical Implementation

The previous sections describe the electron field equations for a zero-electron-inertia hybrid simulation scheme. The physics contained in these equations is not new; similar equations have formed the basis of numerous analytical and numerical models—typically one dimensional or with other simplifying assumptions. However, properly implemented in a two- or higher-dimensional simulation code, these equations can produce an algorithm which provides access to the nonlinear behavior of a wide variety of realistic plasma configurations. The key lies in producing an algorithm which provides flexibility, robustness, and relative ease in setting up new configurations. This larger task is what is now addressed.

In the remainder of this section, it is assumed that the magnetic components B_r, B_θ, and B_z have just been used at time level n to push the ion simulation particle quantities ρ and $\mathbf{u}_i$ to time level $n+1$. Calling the electron–field routine to advance the field components and $\mathbf{u}_e$ to the same time level begins by initiating the following sequence of operations. First, u_{er} is advanced in time by Eq. (9a) using the time levels given schematically by

$$u_{er}^{n+1} = f(\rho^{n+1}, u_{ir}^{n+1}, B_\theta^n). \tag{10a}$$

The next operation is the first half or r pass, in this case, of an ADI time advance. The terms in Eq. (6) which contain spatial derivatives in the r directions (here denoted by R_{terms}) are advanced implicitly one helf time step using the θ-component of **A** and its z derivatives (denoted by Z_{terms}) as source terms. This procedure is represented schematically by

$$\frac{A_\theta^{n+1/2}}{\cdot\cdot/2} + R_{\text{terms}}(u_{er}^{n+1}, A_\theta^{n+1/2}) = \frac{A_\theta^n}{\cdot\cdot/2} - Z_{\text{terms}}(u_{e\cdot}^n, A_\theta^n), \tag{10b}$$

Now the second half of the ADI scheme, described here as the z pass, is made on Eq. (6) to obtain a temporary value of the θ-component of the vector potential $\hat{A}_\theta$ at the time level $n+1$. All temporary values are labeled with $\hat{}$. The result of the r pass equation (10b) provides the required source terms for the second half time step. This step is denoted by

$$\frac{\hat{A}_\theta}{\Delta t/2} + Z_{\text{terms}}(u_{ez}^n, \hat{A}_\theta) = \frac{A_\theta^{n+1/2}}{\Delta t/2} - R_{\text{terms}}(u_{er}^{n+1}, A_\theta^{n+1/2}). \tag{10c}$$

This temporary value of $\hat{A}_\theta$ is now used to provide intermediate values for the r- and z-components of $\mathbf{B}$ (both components are here represented by $\hat{B}$) by taking the curl

$$\hat{B} = \nabla \times \hat{A}_\theta \hat{e}_\theta. \tag{10d}$$

The θ-component of $\mathbf{u}_e$ is obtained by using Eq. (9b):

$$\hat{u}_{e\theta} = f(\rho^{n+1}, u_{i\theta}^{n+1}, \hat{A}_\theta). \tag{10e}$$

Now the r pass on the B_θ can be conducted with a similar schematic representation given by

$$\frac{B_\theta^{n+1/2}}{\Delta t/2} + R_{\text{terms}}(u_{er}^{n+1}, B_\theta^{n+1/2}) = \frac{B_\theta^n}{\Delta t/2} - Z_{\text{terms}}(u_{ez}^n, B_\theta^n) + f(\hat{u}_{e\theta}, \hat{B}, T_e) \tag{10f}$$

followed by an application of Eq. (9c) to obtain u_{ez},

$$u_{ez}^{n+1} = f(\rho^{n+1}, u_{iz}^{n+1}, B_\theta^{n+1/2}), \tag{10g}$$

so that the z pass of the B_θ time advance can be completed:

$$\frac{B_\theta^{n+1}}{\Delta t/2} + Z_{\text{terms}}(u_{ez}^{n+1}, B_\theta^{n+1}) = \frac{B_\theta^{n+1/2}}{\Delta t/2} - R_{\text{terms}}(u_{er}^{n+1}, B_\theta^{n+1/2}) + f(\hat{u}_{e\theta}, \hat{B}, T_e). \tag{10h}$$

Finally, the final z pass is made on A_θ with the time advanced u_{ez} for the convective term

$$\frac{A_\theta^{n+1}}{\Delta t/2} + Z_{\text{terms}}(u_{ez}^{n+1}, A_\theta^{n+1}) = \frac{A_\theta^{n+1/2}}{\Delta t/2} - R_{\text{terms}}(u_{er}^{n+1}, A_\theta^{n+1/2}) \tag{10i}$$

followed by a final updating of B_r, B_z, and $u_{e\theta}$ given by

$$B_{r,z}^{n+1} = \nabla \times A_\theta^{n+1} \tag{10j}$$

and

$$u_{e\theta} = f(\rho^{n+1}, u_{i\theta}^{n+1}, A_\theta^{n+1}). \tag{10k}$$

The above sequence of operations constitutes a noniterative alternating direction implicit time advance of Eqs. (6) and (7) which is second order accurate in Δt for B_θ and A_θ and therefore for B_r and B_z. This sequence of steps has been so chosen that it confirms as nearly as possible to the "conventional wisdom" of nonlinear ADI [8]. First note that the updates of the electron r and z drift velocities are so arranged that an update occurs before its nonlinear *implicit* use. To update a nonlinear coefficient immediately before its explicit use would adversely effect stability. Second, for nonlinear variables such as $u_{e\theta}$ which do not occur as coefficients of the unknown, the variable update should be carried out only at such times that the numbers of r passes and z passes are equal. This is the reason for the creation in Eq. (10c) and use in Eqs. (10d) and (10e) of the temporary $\hat{A}_\theta$. To neglect operation (10c) and replace $\bar{A}_\theta$ in the next two equations by $A_\theta^{n+1/2}$ from (10b) increases the numerical diffusion significantly and appears to make the overall algorithm less robust.

A smoothing of A_θ in all vacuum regions is carried out between steps (10i) and (10j). This operation is performed by solving $\nabla^2 \mathbf{A}|_\theta = 0$ in these regions, again using adaptive ADI. Since A_θ has already been advanced in time, this step smooths some oscillations which develop due to the noniterative ADI passes on $\nabla^2 \mathbf{A}|_\theta = 0$.

The only fully advanced electron drift velocity component resulting from this algorithm is $u_{e\theta}$. The other two components must *not* be fully advanced or the stability of the algorithm will suffer and numerical diffusion will be increased. Consequently, a fully updated set of electron drift velocities is calculated, but not stored, for use in the subsequent evaluation of Eq. (1) for the total **E** field. The sole use of the stored $\mathbf{u}_e$ components is to facilitate the time advance of the magnetic field. The components of $\mathbf{u}_e$ are, however, close enough to the fully advanced values to be entirely satisfactory for diagnostic purposes.

It is also found that the operator combination

$$\frac{\partial}{\partial t} + \frac{\partial}{\partial r} u_{er} + \frac{\partial}{\partial z} u_{ez}, \tag{11}$$

as found in Eq. (7), introduces numerically the equivalent of a term with a negative diffusion coefficient when the space terms are center differenced [9]. Such behavior has often been encountered in explicit fluid dynamic codes and is usually mitigated by using spatial difference approximations which themselves introduce overriding positive numerical diffusion. The need for such techniques has been demonstrated empirically by this implicit formulation as well.

The method of tensor viscosity of Dukowicz and Ramshaw [10] provides a solution to this problem which exhibits significantly less numerical diffusion than earlier techniques. Briefly, the method as applied to the numerical solution of the continuity equation allows the center differencing of spatial terms coupled with a better temporal finite difference approximation of $\partial/\partial t$. Since Eq. (11) does not have all the terms of the cylindrical continuity operator, a new temporal difference operator for use in Eq. (7) was derived which has the form

$$\frac{\partial B}{\partial t} \to \frac{B^{n+1} - B^n}{\Delta t} - \frac{\partial}{\partial r}\left[T_{rr} \frac{\partial B^*}{\partial r} + T_{rz} \frac{\partial B^n}{\partial z} \right] - \frac{\partial}{\partial z}\left[T_{zr} \frac{\partial B^n}{\partial r} + T_{zz} \frac{\partial B^*}{\partial z} \right], \tag{12}$$

where

$$\mathbf{T} = \alpha \frac{\Delta t}{2} \mathbf{u}_e \mathbf{u}_e. \tag{13}$$

The * denotes a time level that may be either n or $n + 1$ depending upon whether the application is in an r or a z pass of the solution process. The α is a constant greater than or equal to unity which provides extra numerical smoothing should it be required. The additional smoothing is still less than that of donor cell techniques [9, 10] until α approaches the electron flow Courant number which can easily be two or three orders of magnitude greater than the corresponding ion Courant number. For the examples presented later, α is set at 100.

All spatial finite difference operators are basically the standard second order forms, and second order derivatives utilize conservative, compact forms. All quantities are assumed to reside at cell centers, which necessitates the definition of ghost cells around the simulation region but greatly eases the problems associated with the application of arbitrary combinations of Dirichlet and Neumann boundary conditions. A standard tridiagonal solver provides the required solutions for the r and z passes of Eqs. (10).

Tests and Applications

To adequately test this model it is necessary to include those plasma configurations which are strongly inhomogeneous (i.e., include vacuum regions) in addition to the usual comparisons with linear theory. Presented here are the results of some tests designed to verify the electron–field algorithm performance in different simplified regimes as well as to demonstrate its more general multidimensional performance. The code ZEMER has been developed to test the algorithm presented in this paper and is used for these tests and applications. This codes makes use of particle moving routines which are direct descendents of the irreversible second order schemes described by Nielson and Lewis [5]. Sgro [4] has adapted this algorithm to the r–z geometry required here. The precise form of the algorithm is immaterial to the method presented in the preceding sections, which assumes only that there is an algorithm which advances the ion component explicitly in time and provides ρ, $\mathbf{u}_i$, and T_i at $t = (n + 1)\Delta t$ given the ion representation as well as $\mathbf{E}$ and $\mathbf{B}$ at time level $t = n\,\Delta t$.

The first test case is a one-dimensional θ-pinch implosion which provides a verification of the time integration of the A_θ equation (6) in a strongly inhomogeneous, nonlinear environment. Complications due to the A_θ, B_θ coupling are largely absent since B_θ is negligibly small. (B_θ would be identically zero were it not for random fluctuations in the ion source terms.) Since analytic methods cannot describe this implosion, the standard of comparison is a similar implosion run on the well-tested one-dimensional hybrid code of Sgro and Nielson [11] which contains similar physics. The algorithms in the two-dimensional code described here are substantially different from those used for the one-dimensional results, so that if the two produce similar physics, a high degree of confidence in the A_θ integration is warranted.

The test problem presented here consists of a homogeneous 1-eV ion plasma with density 3×10^{14} which is subjected to a 5-kG external B_z field at time equal to zero. The electron temperature is also 1 eV and is not allowed to change in time. The ion gyrofrequency in the external field is 2.4×10^7 rad/sec; the Alfvén velocity at cutoff density in the external field is 2.4×10^8 cm/sec. The numerical parameters are: 40 uniform cells in radius $0 < r < 10$ cm, 20 uniform cells in $0 < z < 10$ cm, Δt is 2 ηsec and the total number of particles is 10,000. Shown in Fig. 1a is the resulting $\mathbf{v}_i$ versus r phase space after 200 ηsec from the one-dimensional code. Figure 1b gives the

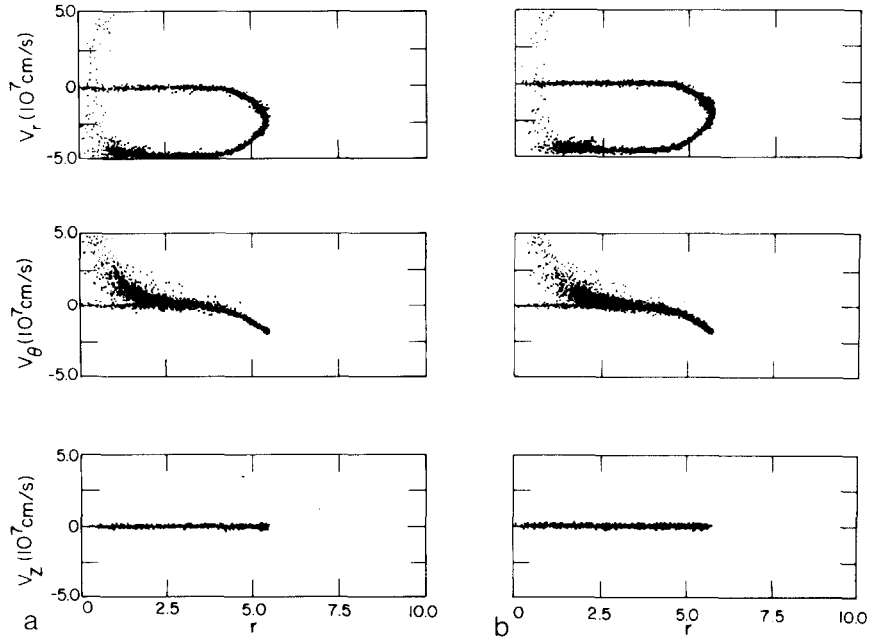

FIG. 1. The ion phase space that results after 200 ηsec. The $t = 0$ configuration consisted of a homogeneous 1-eV deuterium plasma with a density of 3×10^{14} which is subjected to an external B_z implosion field of 5 kG. (a) Result obtained using the one-dimensional algorithm of Sgro and Nielson (courtesy of A. G. Sgro). (b) Result obtained using the two-dimensional algorithm described in the text.

corresponding plot from the two-dimensional code. The implosion velocities agree to within 6%. The addition of various averaging techniques can be employed when evaluating terms in Eqs. (10) which easily provide an order of magnitude improvement in agreement, using the position of the vacuum–plasma interface as the only criterion. With such additions the qualitative agreement of other features that is evident in Fig. 1 is easily degraded. The results presented in this section were obtained with the straightforward application of the ideas presented in the section on numerical implementation. Agreement improves when the number of cells in the radial direction is increased.

The second test provides a similar test of the B_θ equation (7) without interference from the A_θ dependency. This is accomplished by considering a Z-pinch implosion which is initiated by imposing a finite B_θ (again 5 kG) at $r = r_{max}$. This boundary condition numerically induces a z current in the plasma which results in the subsequent implosion. A_θ in this case would be exactly zero were it not again for random noise in the ion source terms. The Z-pinch implosion test is made with numerical parameters similar to those of the first test but with B_θ $(r = 10\text{ cm}) = 5$ kG and B_z $(r = 10\text{ cm.}) = 0$. The ion gyrofrequency in the 200-ηsec field just outside the plasma is roughly 4.8×10^7 rad/sec; the Alfvén velocity at cutoff density in the same 200-ηsec field is 4.9×10^8 cm/sec. The comparison is again made with the v_i versus r

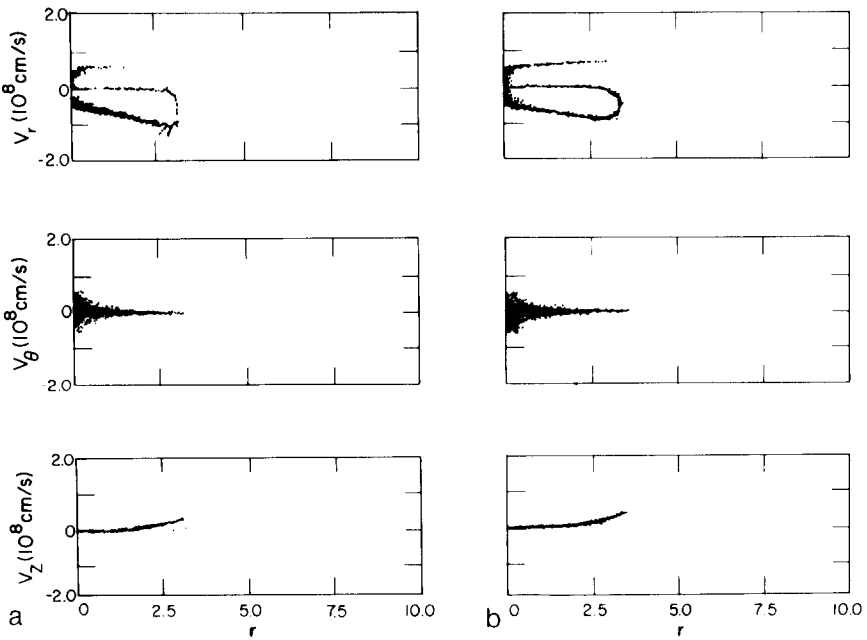

FIG. 2. Result of an implosion driven by a 5-kG external B_θ field with other conditions remaining similar to those described in Fig. 1. (a) Result obtained using the one-dimensional Sgro-Nielson algorithm (courtesy of A. G. Sgro). (b) Result obtained using the two-dimensional algorithm described in the text.

phase space plots obtained with the Sgro–Nielson code. The one-dimensional result in Fig. 2a and the two-dimensional result in Fig. 2b agree to within a few percent.

The third test includes nontrivial two-dimensional effects and therefore full coupling between the A_θ and B_θ Eqs. (6) and (7). Starting with a homogeneous, anisotropic plasma immersed in strong B_z, comparisons can be made with the linear theory for growth of both mirror and ion-cyclotron instabilities [12]. The results presented here are from an ongoing study of nonlinear saturation levels on these modes by Sgro *et al.* [13]. Such a comparison is made difficult by several factors. Possibly the most significant issue is the fact that a cylindrical code is not well suited to the simulation of modes in an infinite homogeneous plasma. This is true for two reasons. First, the best-suited boundary conditions for infinite plasma simulations are periodic boundary conditions, which obviously cannot be applied in the radial direction. This case is particularly difficult in that obliquely propagating modes are expected. Second, with uniform cell spacing in the radius, more plasma mass is present in the outermost cells than in the inner cells by a factor of r. Consequently the simulation fluctuation level (a measure of which is given by the number of simulation particles per cell) is much higher near the axis than on the outside—assuming simulation particles of equal mass.

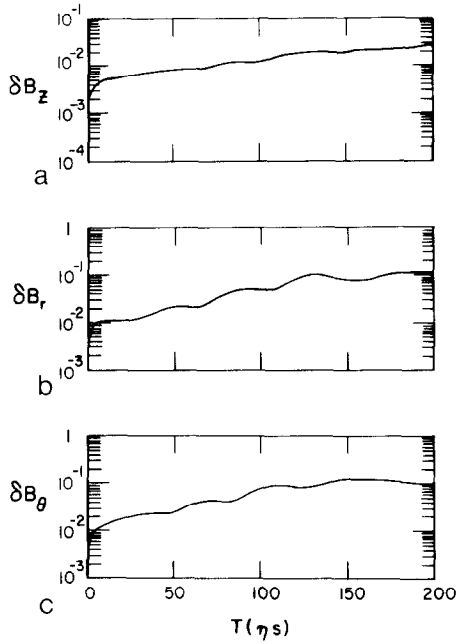

FIG. 3. (a–c) Time history of the turbulent components of the magnetic field. This magnetic field behavior results from an initial plasma configuration which is immersed in a strong (20 kG) homogeneous external B_z and is highly anisotropic ($T_{i\perp}/T_{iz} = 20$). This configuration is unstable to both the mirror instability which is responsible for the turbulent B_z behavior and the ion-cyclotron instability which appears in the turbulent B_r and B_θ behavior.

With these caveats, the preliminary results of a simulation with the following parameters are presented. A homogeneous density of 3×10^{16} with a T_{iz} of 1 keV and $T_i/T_{iz} = 20$ is represented by 80,000 thermally loaded particles. A 20-kG external B_z is imposed on this system. The ion gyrofrequency in the bias field is 9.6×10^7 rad/sec; the Alfvén velocity at cutoff density in this field is 9.8×10^7 cm/sec. The spatial representation contains 40×40 equally spaced grid points in the radial and axial directions which encompass 0 to 10 cm in radius and 0 to 4 cm along the axis. The time step used in these runs was 0.5 ηsec. Figure 3a shows the resulting behavior of the turbulent B_z field as a function of time. From linear theory it is expected that the component of the turbulent B field parallel to the zeroth order field should grow at the mirror growth rate. The theoretical growth rate of the turbulent B_z is 3.2×10^7 and the numerically observed growth rate is 1.6×10^7. The components of B perpendicular to the applied field, shown in Figs. 3b and c, exhibited growth at the ion-cyclotron growth rate, which according to linear theory is 4×10^7. The corresponding value obtained from the simulation is 1.97×10^7. This discrepancy may be due to the fact that there several unstable modes which can share in the free energy available to drive instabilities. There are at least three modes allowed by the boundary conditions which have comparable linear growth rates in this case. Careful selection of the box length in the axial (periodic) direction so that only one of the allowed modes has an appreciable linear growth rate for the mirror instability has yielded almost exact agreement with theory. Unfortunately, such selection of unstable wavelengths is nearly impossible for both mirror and ion-cyclotron instabilities simultaneously. Considering the earlier discussion of the limitations of a cylindrical (r–z) code for this simulation, the agreement is quite acceptable. It should be pointed out that this $t = 0$ homogeneous plasma representation has 11 vacuum cells due to fluctuations. This number varies only slightly during the course of the run but, of course, the locations of these cells exhibit rapid stochastic movement.

The best demonstration of the plasma–vacuum capabilities of this model is simulations of the setup phase of a bumpy θ-pinch shown in Figs. 4a, b, and c. An initially homogeneous Maxwellian ion distribution is imploded by an external B_z field of the form

$$B_z = \left(5 + 2.5 \sin \frac{2\pi}{L} z\right) \text{ kG}.$$

For this run there were 10,000 ions in a 40×40 mesh with dimensions $0 \leqslant r \leqslant 10$ cm and $0 \leqslant z \leqslant 100$ cm and $\Delta t = 2$ ηsec. The number of $t = 0$ vacuum cells is 23. The ion gyrofrequency in the largest external field is 3.7×10^7 rad/sec; the Alfvén velocity at cutoff density in this field is 3.7×10^8 cm/sec. A variety of ion phenomena is evident. In Fig. 4a, the reflected ion beam is about to reach $r = 0$ at approximately $z = 7.5$ cm. The reflected ion beam is beginning to recompress the external field in Fig. 4b. From the several "free" particles, it is evident that from this time forward, the code must respond to an even more complicated intermixing of

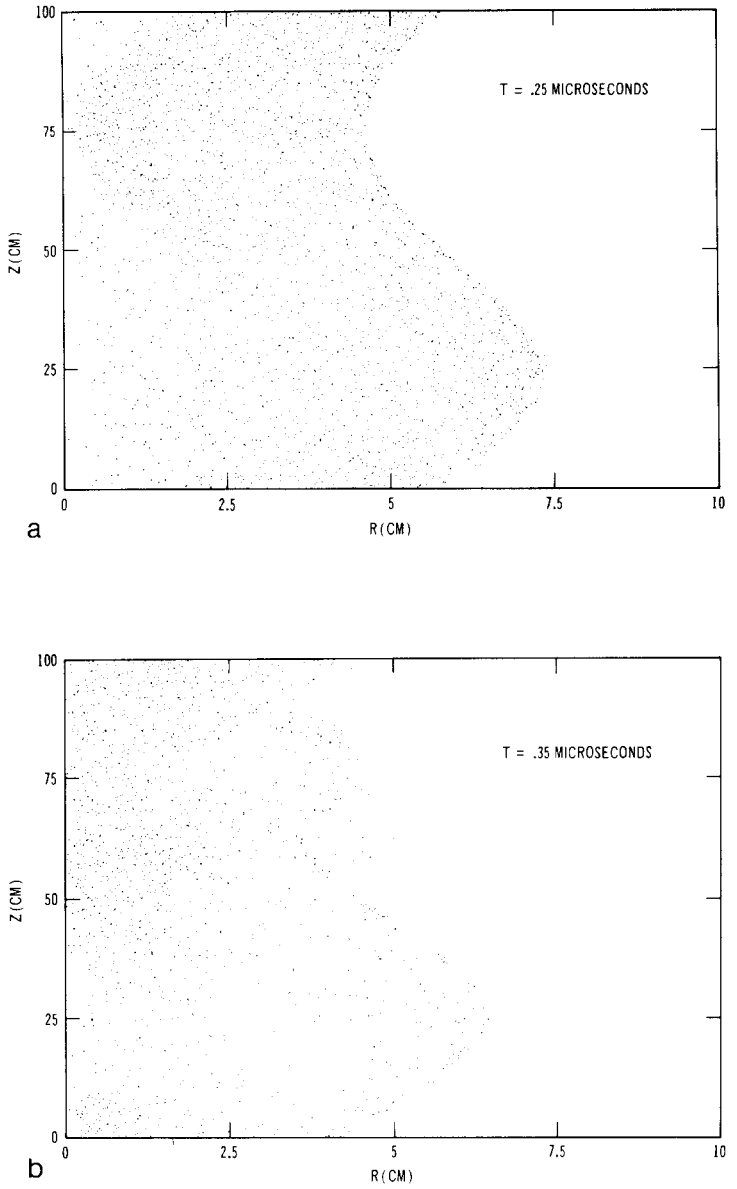

FIG. 4. (a–c) Ion positions in r–z space which result from an initially homogeneous 1-eV plasma being subjected to a bumpy θ-pinch implosion field given by $B_z = 5(1 + 0.5 \sin(2\pi z/L))$ kG. Those ions which actually bounce off of the external field are nearing the axis at $z = 7.5$ cm in (a). In (b), those same ions have reflected from the symmetry plane at $r = 0$ and are starting to recompress the external field. Note the isolated particles. (c) Ion positions at a later time at which the density configuration is still highly turbulent and far from equilibrium.

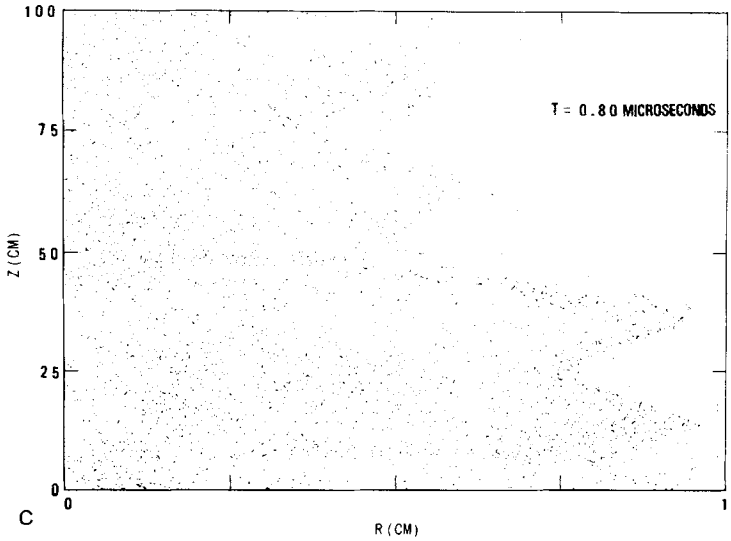

FIG. 4—*Continued.*

plasma and vacuum regions. Figure 4c shows a typical example of such intermixing at a later time. This configuration, however, is still far from equilibrium.

CONCLUSIONS

In this paper an appropriate combination of the electron momentum equation in the zero inertia limit and Maxwell's equations in the radiation-free or Darwin limit has been developed which is suitable for numerical integration in a hybrid simulation code. Next, a method for numerically integrating this combination in concert with the time integration of the ion component is presented. The significant feature of this algorithm is that it provides a practical technique for dealing with the large signal velocities resulting from low density fluctuations that always occur with particle-in-cell techniques. As a result of this capability, it is also possible to correctly treat true vacuum regions—a capability which permits a wide variety of macroscopic applications for this method.

ACKNOWLEDGMENTS

During the course of the work presented in this paper, the author has enjoyed and benefited from discussions with a great many friends and colleagues. Among those to whom a particularly large debt is owed are J. E. Dendy, J. M. Hyman, I. R. Lindemuth, and C. W. Nielson. A most important contribution was made by A. G. Sgro, who provided useful and timely feedback on many issues, and who is largely responsible for many of the particle-in-cell techniques.

REFERENCES

1. H. OKUDA, J. M. DAWSON, A. T. LIN, AND C. C. LIN, *Phys. Fluids* **21** (1978), 476.
2. D. W. HEWETT AND C. W. NIELSON, *J. Comput. Phys.* **29** (1978), 219.
3. J. A. BYERS, B. I. COHEN, W. C. CONDIT, AND J. D. HANSON, *J. Comput. Phys.* **27** (1978), 363.
4. D. W. HEWETT AND A. G. SGRO, *in* "Proceedings, Eighth Conference on Numerical Simulation of Plasmas, Monterrey, California, 1978," Paper PC12.
5. C. W. NIELSON AND H. R. LEWIS, *in* "Particle-Code Methods in the Nonradiative Limit," p. 367, Methods in Computational Physics, Vol. 16, Academic Press, New York, 1976.
6. R. D. RICHTMEYER AND K. W. MORTON, "Difference Methods for Initial-Value Problems," Interscience, New York, 1967.
7. S. DOSS, "Dynamiic ADI Methods for Elliptic Equations with Gradient Dependent Coefficients," Ph. D. dissertation, LBL-6142, April 1977.
8. I. R. LINDEMUTH, "The Animal Code," UCRL-52492, January 1979.
9. C. W. HIRT, *J. Comput. Phys.* **2** (1968), 339.
10. J. K. DUKOWICZ AND J. D. RAMSHAW, "Tensor Viscosity Method for Convection in Numerical Fluid Dynamics," LA UR-78-151; *J. Comp. Phys.*, **32** (1979), 71.

[redacted]

15. A. G. SGRO, D. W. HEWETT, AND T. E. CAYTON, The nonlinear evolution of the ion mirror instability, Paper 1C12, Sherwood Meeting, Mount Pocono, Pa., 1979.